Supporting Material

Pursuing the stabilization of crystalline nanostructured magnetic manganites through a green low temperature hydrothermal synthesis

A. Minelli,[a] P. Dolcet,*[a,b] S. Diodati,[a] S. Gardonio,[c] C. Innocenti,[d] D. Badocco,[a] S. Gialanella,[e] P. Pastore,[a] L. Pandolfo,[a] A. Caneschi,[d] A. Trapananti[f] and S. Gross*[a,b]

Characterisation methods

X-Ray diffraction XRPD patterns were collected with a Bruker D8 Advance diffractometer equipped with a Göbel mirror and employing the CuK_α radiation. The angular accuracy was 0.001°and the angular resolution was better than 0.01°. All patterns were recorded in the range 10–80°with a scan step 0.03° (2θ) and a 7 second per step acquisition time. Patterns of $ZnMnO_3$ and $CuMnO_2$ were analysed through the use of the Scherrer formula[1,2] to obtain an estimation of the crystallites sizes.

Rietveld refinement of powder XRD patterns of $ZnMnO_3$ was carried out using TOPAS Academic v5, in order to understand the atomic positions and the structure of the crystalline phase. The modified Thompson-Cox- Hastings (TCH) pseudo-Voigt profile function was used to model the experimental line shape, convoluted with a simple axial model correction.[3] The quality of the refinement was assessed by the values of the discrepancy factor (profile weighted residual error), R_{wp}.

XPS analysis Zinc manganites were investigated by XPS with a Φ 5600ci Perkin-Elmer spectrometer, using a standard aluminium (Al K_α) source, with an energy of 1486.6 eV operating at 200 W. Crednerite was investigated using a standard magnesium (Mg K_α) source with an energy of 1253.6 eV operating at 220 W. The choice of the magnesium source was dictated by the need to avoid overlapping of Cu 2p core level and Cu $L_2M_{45}M_{45}$ Auger spectra.

The X-ray source employed was located at 54.7° relative to the analyser axis. The working pressure was <5 x 10^{-8} Pa (~10^{-11} torr). The energy calibration was based on the binding energy (BE) of the $Au4f_{7/2}$ core level and the overall energy resolution was 0.15 eV. The reported BE values were corrected for surface charging effects, assigning the BE value of 284.6 eV to the C1s line of carbon.[4–6] The atomic composition, after a Shirley-type background subtraction,[7] was evaluated using sensitivity factors supplied by Perkin-Elmer.[4] The spectra were analysed using the IGOR Pro v. 4.01 program, whereas quantitative analyses were performed using the MultiPak program. The fitting of the Mn 2p peaks was carried out with the XPSPEAK 4.1 freeware program, considering spin-orbit splitting in the 11.05-11.5 eV range ,[4,5] a constant %GL (Gaussian and Lorentzian percentage) and a FWHM with an error of ± 0.2 eV.

ICP–MS analysis Metal composition was determined with an inductively coupled plasma coupled - mass spectrometry Agilent Technologies 7700 ICP-MS system (Agilent Technologies International, Japan, Ltd., Tokyo, Japan). The MS detector was equipped with an octopole collision cell operating in kinetic energy discrimination mode for the removal of polyatomic interferences. The operating conditions and data acquisition parameters are reported in an article by Badocco *et al*.[8] The material was mineralised by treating a suitable amount of sample (about 15 mg) with 5 g of 69% HNO_3. A Microwave Digestion System (CEM EXPLORER SP-PLUS) was used to completely dissolve the samples. The operative conditions were usually: T_{max} = 200°C, pressure = 300 psi, power = 250 W, 5 min ramp to 200°C followed by a 15 minute digestion.

Elemental (CHN) analysis Tests were performed on a Fisons Instruments 1108 CHNS-O elemental analyser.

TEM Powder samples were prepared for transmission electron microscopy (TEM) observations. A small amount of each sample was suspended in ethanol using an ultrasonic bath to eliminate agglomeration. A drop of this suspension was deposited onto a carbon coated gold grid. Images of the microstructure and the relevant selected area electron diffraction (SAED) patterns were acquired using an analytical electron microscope, Philips CM12, operated at 120 keV and equipped with an energy dispersive X-ray spectroscopy (EDXS) analyser (EDAX Falcon, with a C/U detector).

SEM The samples were analysed by a SUPRA 40 VP Zeiss microscope.

X-ray Absorption Mn K-edge (6539 eV) spectra were collected at the Italian BM08 beamline (GILDA)[9] of the European Synchrotron Radiation Facility (ESRF), under standard ring conditions (6.0 GeV, 200 mA).

Spectra were collected using a double-crystal Si(311) monochromator for energy selection and two Pd-coated mirrors working at an incidence angle of 3.6 mrad were used for harmonics rejection.

Data collection was carried out in transmission mode using two ionisation chambers. The energy scale was continuously monitored by simultaneous absorption measurement on a metallic Mn foil placed between two ionisation chambers located after the sample. Each sample was prepared as a pellet, using cellulose as a binder.
SQUID Magnetic properties of the materials were investigated using a Quantum Design MPMS SQUID magnetometer, operating in the 1.8 K – 350 K temperature range, with an applied field up to 50 KOe. zfc/fc magnetizations were recorded after cooling the sample in the absence (zfc) or presence (fc) of a 50 Oe probing field. Measurements were performed on powder samples, hosted in a Teflon sample holder. The analyses were carried out at Università di Firenze.

Synthesis protocols

Table S1 Different synthesis protocols for the preparation of three compounds.

Sample	Zn or Cu[a]	Mn1[a,b] precursors	Mn2	Nominal (Zn or Cu)/Mn/oxalic acid molar ratio	Treatment T	time	Output
$ZnMn_2O_4$							
ZnMn001	**$Zn(NO_3)_2$**	**$Mn(OAc)_2$**	**-**	**1/1/2**	**180°C**	**24 h**	**presence of ~ 40% of ZnO and 60% of $ZnMn_2O_4$**
ZnMn002	$Zn(NO_3)_2$	$Mn(OAc)_2$	-	1/1/2	200°C	24 h	higher amount of ZnO with respect to ZnMn001
ZnMn003	$Zn(NO_3)_2$	$Mn(OAc)_2$	-	1/1/1	180°C	24 h	higher amount of ZnO with respect to ZnMn001
ZnMn006	$Zn(NO_3)_2$	$Mn(OAc)_2$	-	1/1/1	200°C	24 h	higher amount of ZnO with respect to ZnMn001
ZnMn007	$Zn(NO_3)_2$	$Mn(OAc)_2$	-	1/1/2	180°C	48h	~ amount of ZnO with respect to ZnMn001
ZnMn010	$Zn(NO_3)_2$	$Mn(OAc)_2$	-	0.6/1/2	180°C	24 h	~ amount of ZnO with respect to ZnMn001
$ZnMnO_3$							
ZnMn004	$ZnCl_2$	$MnCl_2$	$KMnO_4$	1/1/1	180°C	24 h	spurious phases
ZnMn005	**$ZnCl_2$**	**$MnCl_2$**	**$KMnO_4$**	**1/1/2**	**180°C**	**24 h**	**pure crystalline phase**
$CuMnO_2$							
CuMn001	**$Cu(NO_3)_2$**	**$Mn(OAc)_2$**	**-**	**1/1/2**	**180°C**	**24 h**	**pure crystalline phase**

[a] Hydrated salt[b] The Mn total molar amount is split into 60% molar Mn1 reagent and 40% molar Mn2 reagent

XPS Analysis

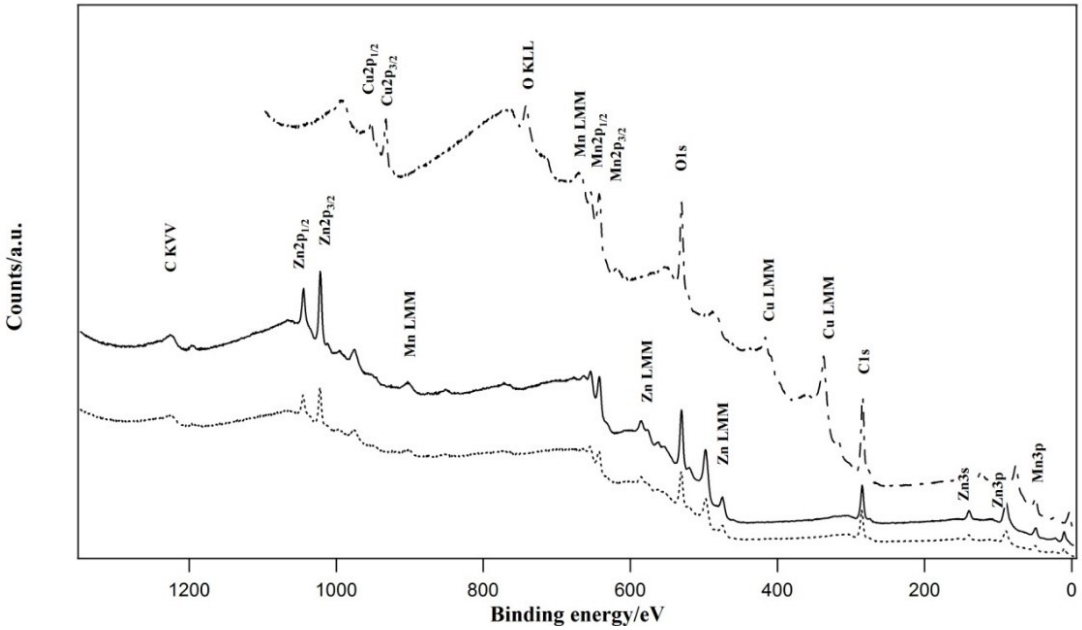

Figure S1 XPS spectra of $ZnMnO_3$ (dotted line), $ZnMn_2O_4$ (continuous line) and $CuMnO_2$ (dash and dot line) with main peaks indexed (BE corrected for charging effect)

In **Figure S2,** the XPS spectra of Zn 2p core levels for the spinel manganites, $ZnMn_2O_4$ and $ZnMnO_3$ are shown. The spectra have the same line shape and the peaks are at the same binding energy. The Zn 2p binding energies, as well as the calculated Auger parameter, see Table 3 in main text,[4,10,11] are in agreement with Zn^{II} in an oxidic environment.[5,12–15] The ZnO phase present in the $ZnMn_2O_4$ is difficult to distinguish from the spinel phase, since both Zn 2p binding energy and Auger parameters are very similar.

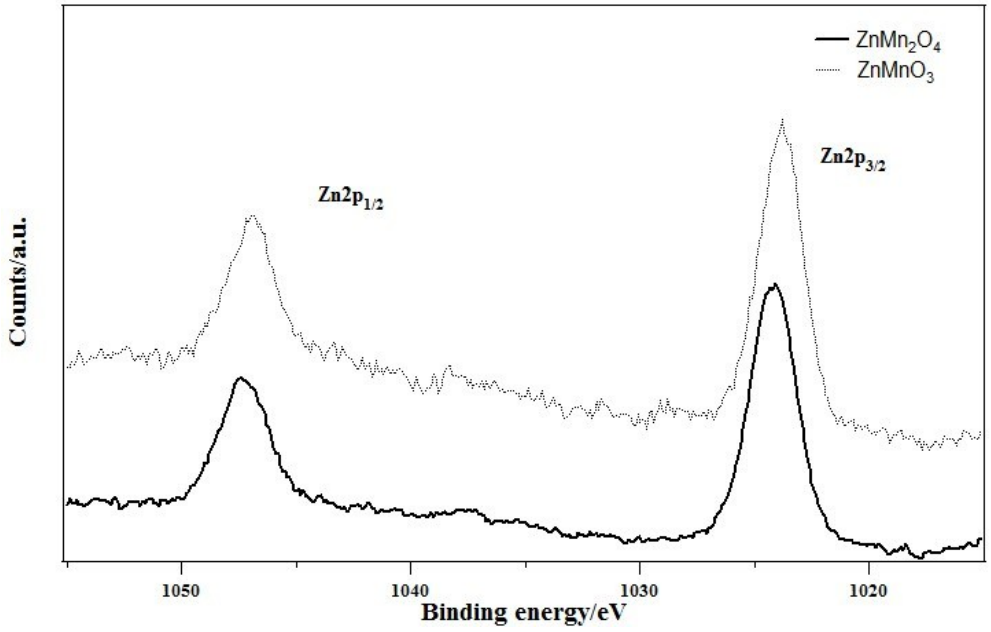

a)

Figure S2 Zn 2p core level spectra measured on the two spinel manganites, $ZnMnO_3$ (dotted line) and $ZnMn_2O_4$ (continuous line).

Concerning the crednerite ($CuMnO_2$) phase, the Cu 2p core level binding energy and the $CuL_3M_{23}M_{23}$ Auger peak energy suggest that copper is in a single oxidation state (*i.e.* Cu^{I}). This is in agreement with the results reported by Töpfer *et al.*,[16] where the crystalline structure of $CuMnO_2$ was described. Specifically, the observed BE values of Cu

2p are compatible with monovalent copper in Cu-type delafossites, such as copper ferrite $CuFeO_2$, multiferroic $CuCrO_2$[17–19] and crednerite thin film.[20,21]

Table S2 Binding energy of Mn 2p core levels measured by different authors with the corresponding oxidation states.

Manganese cation	Mn $2p_{3/2}$	Mn $2p_{1/2}$	Reference
Mn^{II}	639.8	651.3	20
	640.3		22
	640.9		23
	641.0	653.0	24
Mn^{III}	641.1	652.5	20
	641.2		23
	641.3		25
	641.4		22
	641.8	653.4	24
	642.4	654.4	26
Mn^{IV}	641.9		23
	642.6		22
	642.7		25
	643.3	654.6	24
	643.4	653.7	20
Mn^{VII}	647.0		27

In **Figure S3**, the valence band spectra of cubic spinel $ZnMnO_3$ and copper manganite are reported. In the case of $CuMnO_2$, there is a main peak centred at about 3.0 eV BE with a less intense, broad peak at about 7 eV BE. In the case of the cubic spinel $ZnMnO_3$, a main feature is visible at 10.0 eV BE.

The valence band of copper manganite has already been reported in the literature, and interpreted according to experimental and modelling studies.[20,28] Chen *et al.* examined the valence band in thin film crednerite-$Cu_{1.1}Mn_{0.9}O_2$ samples,[20] with results similar to the valence band in our own compound. Based on the calculations by Jia *et al.*,[28] the peak at higher binding energy could be ascribed to the Mn 3p orbital and the main peak is attributed to the Cu 3d orbital in an oxidation state of I,[16] and located between 0.5 and 3 eV BE. The lower energy spectral feature could be attributed to the O 2p orbital.[20,28–30]

The valence band spectrum of cubic spinel $ZnMnO_3$ present a peak at 10 eV BE and a low spectral intensity in the energy region 2-6 eV. The spectrum here shown is the first reported measurement of the valence band of this compound, while the calculated Density of States has been done for $ZnMn_2O_4$ in relation to different *c/a* crystal cell parameter ratios.[31] In the measured spectrum (Fig. S3), we attribute the main peak at 10 eV BE to Zn 3d states and the spectral region 2-6 eV BE to O 2p states.

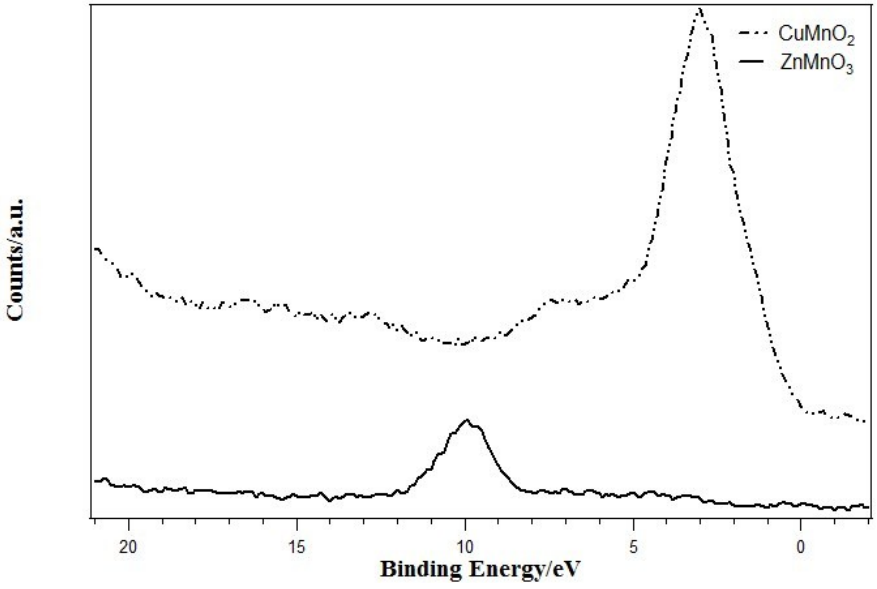

Figure S3 Valence band spectra of $ZnMnO_3$ (continuous line) and $CuMnO_2$ (dash and dot line)

TEM-SAED characterization

$ZnMn_2O_4$

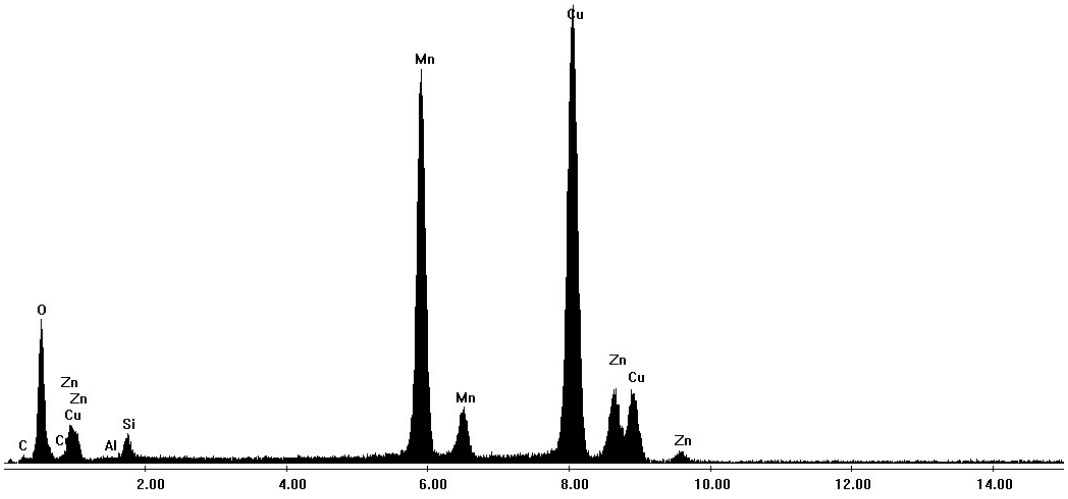

a)

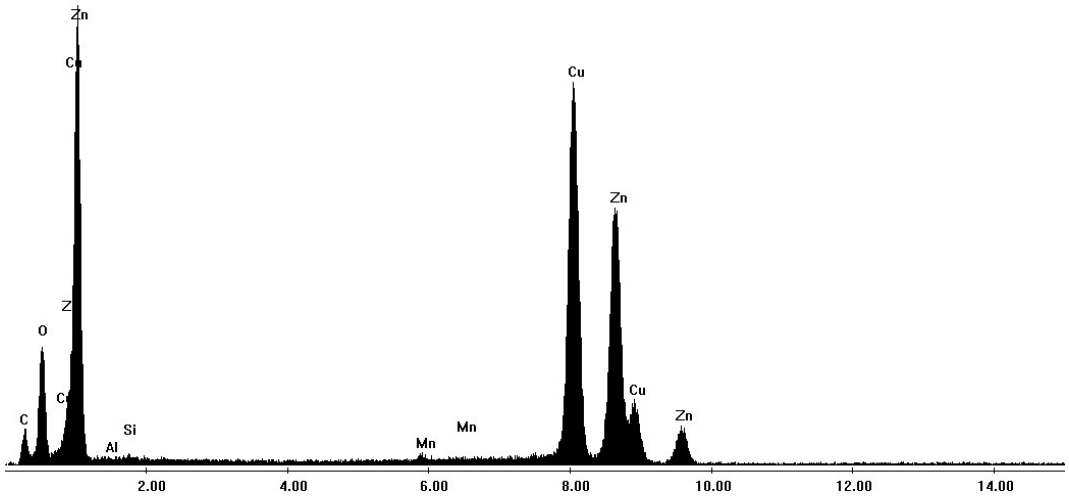

b)

Figure S4 EDXS results from ZnMn001 sample, (a) refers to $ZnMn_2O_4$ grains and (b) refers to rod-like ZnO. Zn and O elements are present in the two, and Mn in (a), confirming the biphasic ZnMn001 sample. C e Cu are from the carbon coated copper grid, used form sample preparation, whereas Si is mostly coming from the detector inner fluorescence.

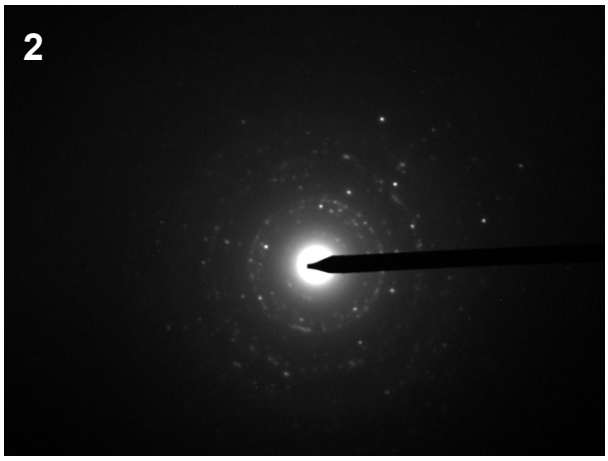
2

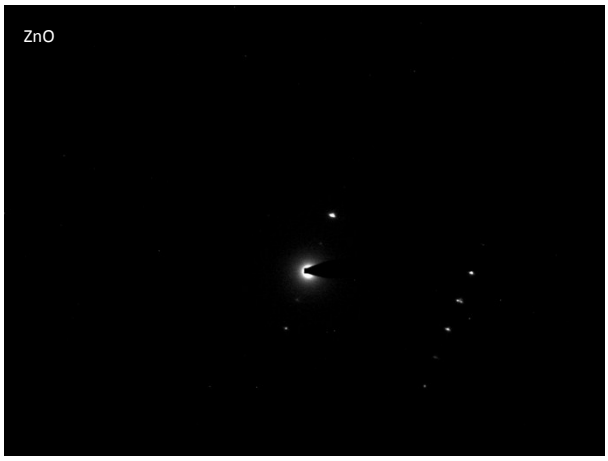
ZnO

c)

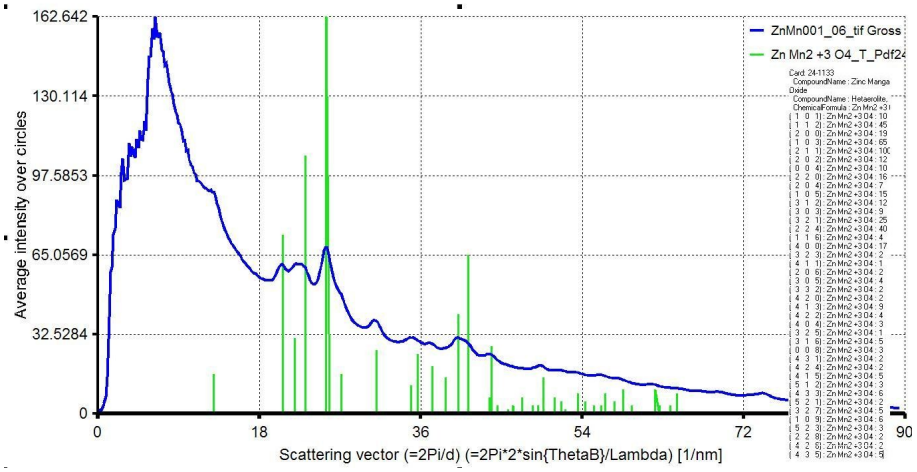

Figure S5 SAED from ZnMn001 sample, (a) refers to $ZnMn_2O_4$ grains and (b) refers to rod-like ZnO. (c) is the plot intensity obtained with the Process Diffraction software, including the relevant indexing in the inset on the right. It confirms that the grains are made of the oxide phase to $ZnMn_2O_4$. For the full crystallographic characterization of the ZnO phase, see data in **Figure S6**.

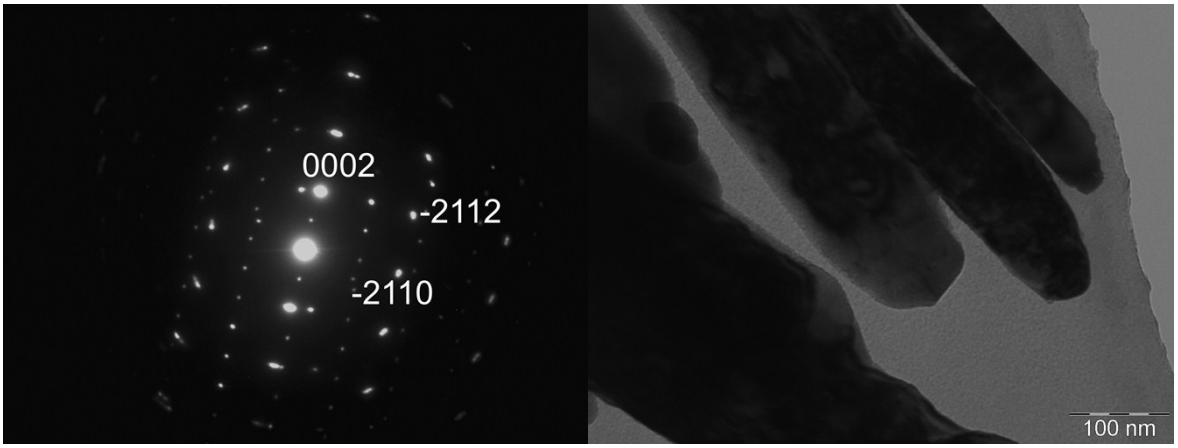

Figure S6 ***ZnO characterization.*** The above SAED pattern is obtained from the grains on the right. For this reason, several sets of slightly misoriented set of diffraction spots are visible. All of them can be indexed according to the hexagonal structure of ZnO, and a coherent indexing is shown. From these set of data, it turns out that the main axis of the rod-like ZnO grains is aligned along the [0001] direction of the hexagonal cell.

$ZnMnO_3$

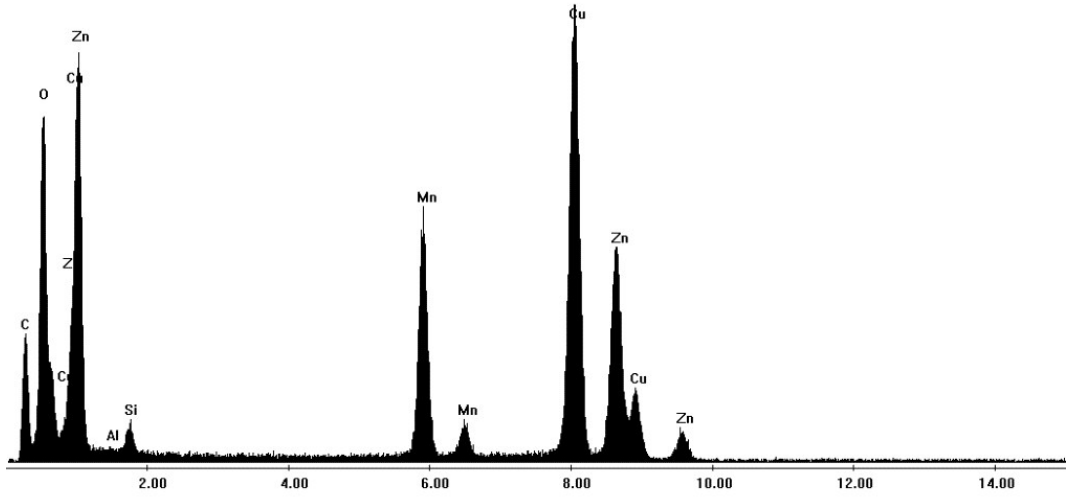

Figure S7: EDXS example of results from ZnMn005 sample ($ZnMnO_3$): homogeneous composition, confirming the presence of Zn, Mn, O elements and the present of a unique and pure phase.

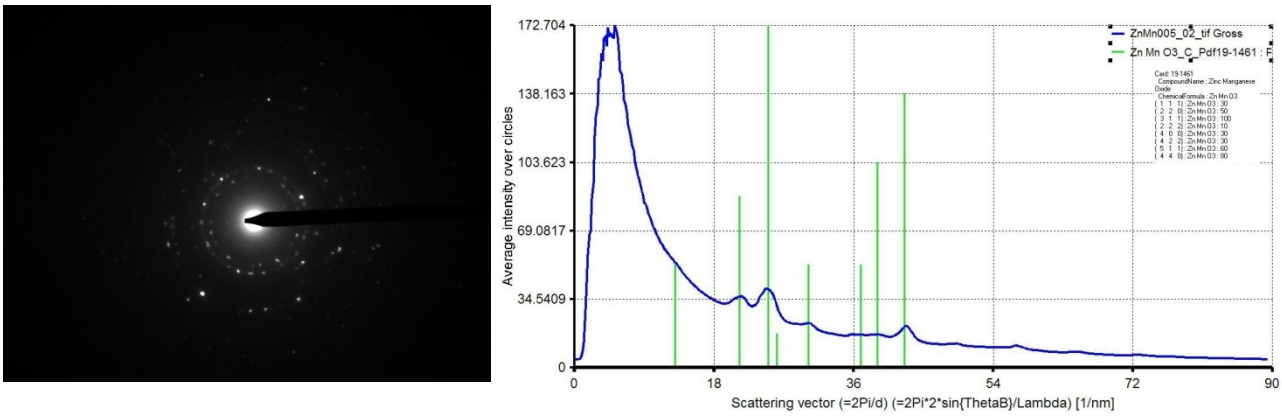

a) b)

Figure S8 (a) SAED pattern of $ZnMnO_3$ phase and (b) intensity plot of the same pattern as obtained from Process Diffraction software, including the relevant indexing in the top right inset.

$CuMnO_2$

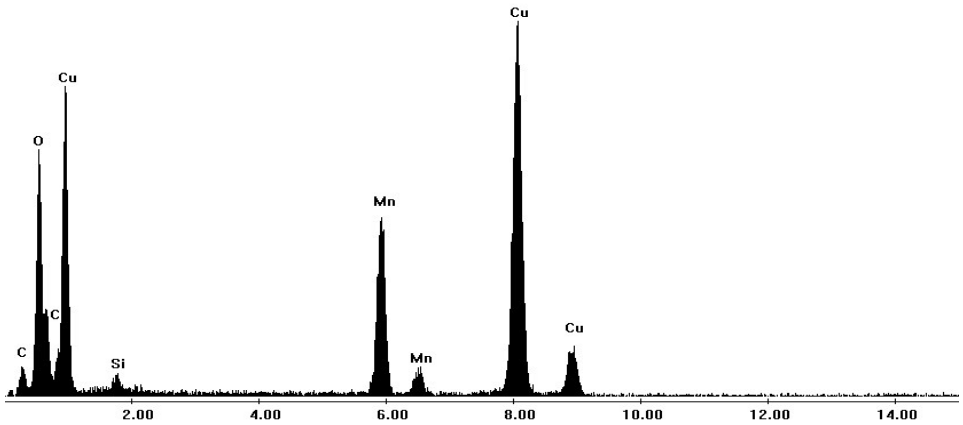

Figure S9 EDXS example of results from CuMn001 sample ($CuMnO_2$): homogeneous composition, confirming the presence of Cu, Mn, O elements and the present of a unique and pure phase.

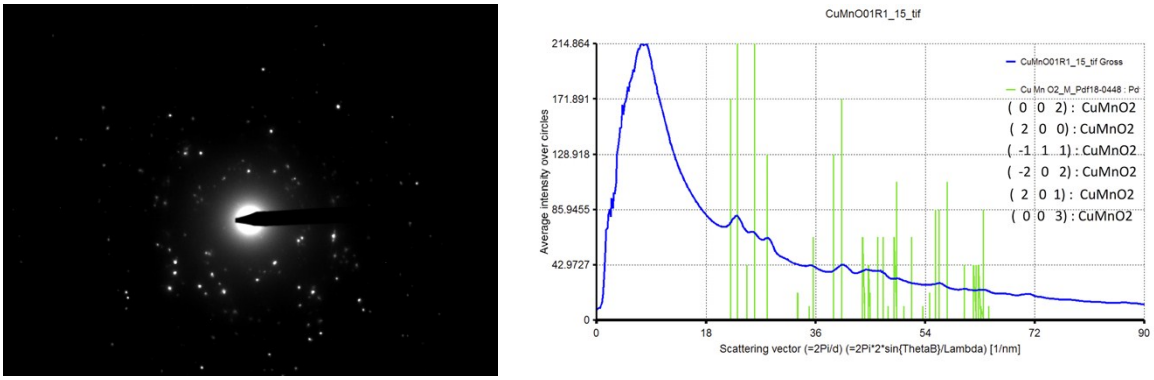

a) b)

Figure S10 (a) SAED pattern of $CuMnO_2$ phase and (b) intensity plot of the same pattern as obtained from Process Diffraction software, including the relevant indexing in the top right inset.

References

1. P. Scherrer, *Nachrichten von der Gesellschaft der Wissenschaften zu Göttingen, Math. Klasse*, 1918, **2**, 98–100.

2. H. P. Klug and L. E. Alexander, *X-ray diffraction procedures for polycrystalline and amorphous materials*, John Wiley & Sons, New York, 2nd edn., 1974.

3. R. A. Young and R. A. Young, *The Rietveld Method*, Oxford University Press, 1995.

4. J. F. Moulder, W. F. Stickle, P. E. Sobol, and K. D. Bomben, *Handbook of X-Ray Photoelectron Spectroscopy*, Physical Electronics Inc., Eden Praire, 1992.

5. A. V Naumkin, A. Kraut-Vass, S. W. Gaarenstroom, and C. J. Powell, *NIST Stand. Ref. Database 20, Version 4.1*, 2012, http://srdata.nist.gov/xps/.

6. D. Briggs and P. Seah, *Practical Surface Analysis, Auger and X-ray Photoelectron Spectroscopy*, Wiley, 1990.

7. D. Shirley, *Phys. Rev. B*, 1972, **5**, 4709–4714.

8. D. Badocco, I. Lavagnini, A. Mondin, and P. Pastore, *Food Chem.*, 2015, **177**, 147–51.

9. F. D'Acapito, A. Trapananti, S. Torrengo, and S. Mobilio, *Not. Neutroni e Luce di Sincrotrone*, 2014, **19**, 14–23.

10. C. D. Wagner, *Faraday Discuss. Chem. Soc.*, 1975, **60**, 291–300.

11. C. Wagner, M. R. Berman, and R. N. Zare, *Anal. Chemsitry*, 1975, **47**, 1201–1203.

12. S. Diodati, University of Padova, 2013.

13. A. A. Tahir and K. G. U. Wijayantha, *J. Photochem. Photobiol. A Chem.*, 2010, **216**, 119–125.

14. S. Bera, A. A. M. Prince, S. Velmurugan, P. S. Raghavan, R. Gopalan, G. Panneerselvam, and S. V Narasimhan, *J. Mater. Sci.*, 2001, **36**, 5379–5384.

15. A. Bardhan, C. K. Ghosh, M. K. Mitra, G. C. Das, S. Mukherjee, and K. K. Chattopadhyay, *Solid State Sci.*, 2010, **12**, 839–844.

16. J. Töpfer, M. Trari, P. Gravereau, J. P. Chaminade, and J. P. Doumerc, *Zeitschrift für Krist.*, 1995, **210**, 184–187.

17. H.-Y. Chen and K.-P. Chang, *ECS J. Solid State Sci. Technol.*, 2013, **2**, P76–P80.

18. H.-Y. Chen and J.-H. Wu, *Appl. Surf. Sci.*, 2012, **258**, 4844–4847.

19. H.-Y. Chen and J.-H. Wu, *Thin Solid Films*, 2012, **520**, 5029–5035.

20. H.-Y. Chen and D.-J. Hsu, *J. Alloys Compd.*, 2014, **598**, 23–26.

21. H.-Y. Chen and D.-J. Hsu, *Appl. Surf. Sci.*, 2014, **290**, 161–166.

22. B. Gillot, S. Buguet, E. Kester, C. Baubet, and P. Tailhades, *Thin Solid Films*, 1999, **357**, 223–231.

23. A. J. Nelson, J. G. Reynolds, and J. W. Roos, *J. Vac. Sci. Technol. A Vacuum, Surfaces, Film.*, 2000, **18**, 1072.

24. J. Töpfer, A. Feltz, D. Gräf, B. Hackl, L. Raupach, and P. Weissbrodt, *Phys. Status Solidi*, 1992, **134**, 405–415.

25. J. S. McCloy, C. Leslie, T. Kaspar, W. Jiang, and R. K. Bordia, *J. Appl. Phys.*, 2012, **111**, 07E149.

26. S. Åsbrink, A. Waśkowska, L. Gerward, J. Staun Olsen, and E. Talik, *Phys. Rev. B*, 1999, **60**, 12651–12656.

27. Y. Umezawa and C. N. Reilley, *Anal. Chem.*, 1978, **50**, 1290–1295.

28. T. Jia, G. Zhang, X. Zhang, Y. Guo, Z. Zeng, and H. Q. Lin, *J. Appl. Phys.*, 2011, **109**, 07E102.

29. H. Hiraga, T. Fukumura, A. Ohtomo, T. Makino, A. Ohkubo, H. Kimura, and M. Kawasaki, *Appl. Phys. Lett.*, 2009, **95**, 32109.

30. H. Hiraga, T. Makino, T. Fukumura, H. Weng, and M. Kawasaki, *Phys. Rev. B*, 2011, **84**, 41411.

31. H. Choi, J. Shim, and B. Min, *Phys. Rev. B*, 2006, **74**, 172103.